WORLD CONFERENCE ON TIMBER ENGINEERING 2025
BRISBANE, AUSTRALIA
Advancing Timber for the Future Built Environment

STATIC LOADING TESTS OF THE SINGLE-STORY CLT ROCKING SHEAR WALL STRUCTURE

So Momose[1], Takuya Tsuji[2], Takafumi Nakagawa[3], Hiroshi Isoda[4]

ABSTRACT: Instead of the installation of expensive and high-performance hardware employed in CLT panel construction methods, a structure utilizing cost-effective hardware typically used for Japanese conventional houses is proposed in this paper. This system is designed to ensure no damage under moderate seismic events while relying on restoring forces to resist collapse during massive seismic events. This study aims to obtain fundamental insights into the lateral resisting mechanism and collapse limits. To this end, a single-story full-scale CLT building equipped with existing residential hardware was subjected to deformation exceeding 33%. The experimental results confirmed the addition of lateral resistance by hardware, a consistent negative slope of elastic restoring forces, and collapse limit displacement of over 910mm. Furthermore, it was observed that rocking behavior caused the weight concentration on the CLT walls. These findings were verified by numerical analysis.

KEYWORDS: CLT rocking shear wall, Full-scale static loading test, Restoring force, Collapse limit

1 – INTRODUCTION

When CLT panels are used as bearing walls in low-rise buildings, they do not fail due to vertical loads under typical weight settings, but they rock against lateral forces. Supposing the large collapse limit due to rocking can prevent collapse during large earthquakes, the CLT tensile joints should be designed only for moderate earthquakes, and expensive hardware with toughness would be unnecessary. An unexplored point in such a design is the collapse limit of buildings using CLT. Although the authors have brought a CLT building to large deformation and traced the results analytically[1], this is still only one example. Moreover, it is thought that ordinary buildings have walls of different widths, but in such cases, the vertical load distribution and collapse limit deformation, which is the key to the resistance mechanism, has yet to be clarified. In this study, single-story box-shaped specimens with CLT rocking shear walls of different widths were subjected to static forces up to the interstory drift angle of 33% or more to obtain a basic knowledge of the resistance mechanism against lateral forces, the collapse limit, and the axial force for the CLT walls.

2 – SPECIMEN DESIGN AND ELEMENT TESTS OF TENSILE HARDWARE

2.1 SPECIMEN DESIGN

Here, it is assumed that CLT shear walls are used in buildings of approximately two stories. When a shear force is applied, the wall rocks without itself being damaged, as shown in Figure 1. In this case, the wall capacity is determined by the restoring force due to vertical loads and the capacity and stiffness of the tensile hardware. Based on the moment equilibrium at the rotation center, the allowable strength of the wall can be determined using Equation (1).

$$Q = (T + W)\,D\,/\,h\,/\,\alpha \tag{1}$$

If the inflection point height ratio α is known, the allowable capacity for the wall is determined by the

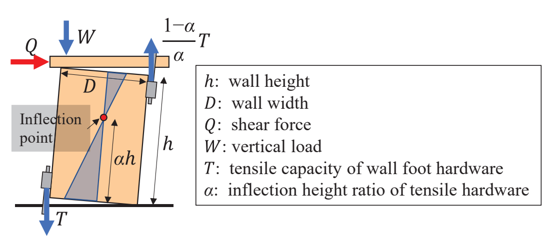

Figure 1. Resisting system of this structure

[1] So Momose, RISH, Kyoto University, Uji, Japan, momose.so.72w@kyoyto-u.ac.jp

[2] Takuya Tsuji, RISH, Kyoto University, Uji, Japan, takuya_tsuji@rish.kyoto-u.ac.jp

[3] Takafumi Nakagawa, RISH, Kyoto University, Uji, Japan, nakagawa@rish.kyoto-u.ac.jp

[4] Hiroshi Isoda, RISH, Kyoto University, Uji, Japan, hisoda@rish.kyoto-u.ac.jp

https://doi.org/10.52202/080513-0010

allowable capacity for the tensile hardware and the vertical loads. Here, considering the performance of CLT shear walls and the hardware used in post-and-beam construction, the tensile hardware is sometimes attached to the end grain of the cross layers, resulting in different stiffness and strength characteristics. To determine the allowable capacity of the wall using Equation (1), it is first necessary to understand the tensile performance of the hardware attached to the cross layers of CLT in the vertical direction. Therefore, tests (simple tensile tests) were conducted. Additionally, since CLT shear walls exhibit rocking behavior, rocking tensile tests were also performed to simulate a more realistic condition.

2.2 SIMPLE TENSILE TEST AND ROCKING TENSILE TEST OF HARDWARE

A monotonic tensile force was applied in the vertical upward direction in the simple tensile tests, as shown in Figure 2(a). If the CLT is considered as a column, this method is similar to the one presented in the allowable stress design for conventional post-and-beam constructions. Two types of metal hardware were used: angle bracket, specifically the PZ Hyper Slim-II (hereafter “angle bracket"), and hold-down hardware, specifically the FFH-S20 (hereafter "HD hardware"). The number of test specimens was six for each type. The strength grade and thickness of the CLT, as well as the species and dimensions of the foundation, were the same as those used in the full-scale tests, including the upcoming rocking tensile tests. Further details are described in the section on full-scale experiments. On the other hand, in the rocking tensile tests, the test was conducted by applying a unidirectional tensile force at an

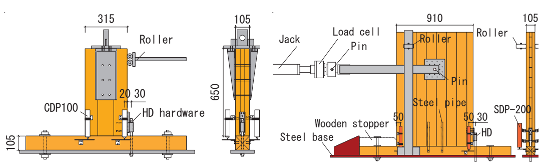

(a) Simple tensile tests (b) Rocking tensile tests

Figure 2. Specimen setup

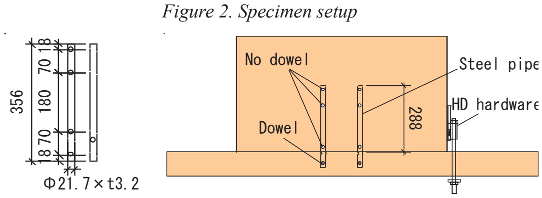

(a) Configuration (b) Installation

Figure 3. The configuration and installation of shear hardware

Table 1. The specimen list

Specimen	Loading height (mm)	Wall width (mm)	Tensile hardware	Shear resistance
910-HS	910	910	HS	A wooden stopper
910-HS-P	910	910	HS	2 steel pipes
1820-HS-P	1820	910	HS	2 steel pipes
910-HDS	910	910	HDS	A wooden stopper
1820-HDS-P	1820	910	HDS	4 steel pipes

arbitrary loading height, as shown in Figure 2(b). Roller supports were installed to clamp the CLT shear wall to prevent out-of-plane deformation. The lateral force was measured by the load cell at the tip of the jack, while the uplift deformation and deformation angle of the CLT shear wall were measured using displacement transducers attached to the wall foot.

The test parameters included the type of tensile hardware, loading height, and shear resistance method. The tensile hardware consisted of the aforementioned angle bracket and HD hardware. The loading heights were set at 910 mm and 1820 mm to examine the effect of shear force magnitude. Regarding shear resistance, in Japanese conventional post-and-beam construction, tenons provide resistance against shear forces in columns. However, tenons were not used to simplify processing in CLT shear walls. Instead, as shown in Figure 3, steel pipes were used. These steel pipes were fixed only to the sill using dowels (denoted as DP in the figure, φ12, L=103). Since steel pipes are expected to contribute to tensile resistance as deformation progresses, an alternative shear resistance method was considered for cases where steel pipes were not used. This method relied on partial compression of the CLT wall foot and stoppers made of cypress lumber. These conditions are summarized in Table 1. The naming convention for the test specimens follows this format: (Loading height) - (Tensile hardware: HS for angle bracket, HDS for HD hardware) - (Presence of shear hardware, denoted by P if present). Each test condition was performed on two specimens. Additionally, the nuts of the HD hardware were hand-tightened.

2.3 TENSILE TEST RESULTS

The simple and the rocking tensile tests exhibited rotational behavior, as shown in Figure 4. Therefore, the uplift deformation δ in the below examination was determined as the vertical displacement at the hardware position, measured using displacement transducers

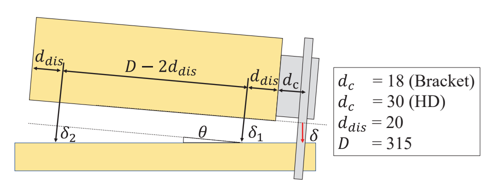

(a) Simple tensile tests

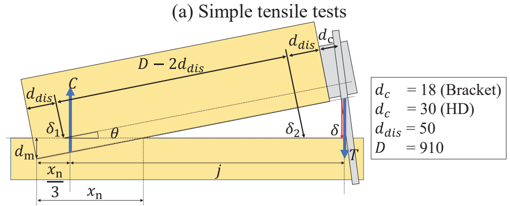

(b) Rocking tensile tests

Figure 4. Diagram of the simple and rocking tensile tests

installed on both sides. In rocking tensile tests, the moment was calculated by multiplying the lateral force by the loading height, and the tensile force for the hardware was obtained by dividing the moment by the moment arm length j, as indicated in Figure 4. The derivation methods for θ, d_{m}, x_{n}, and j are presented below. These derivation methods were also applied in the full-scale experiment where the wall width D was 910 mm or 1820 mm.

$$\theta = \tan^{-1}\left(\frac{\delta_2 - \delta_1}{D - 2d_{\mathrm{dis}}}\right) \tag{2}$$

$$d_{\mathrm{m}} = \left(d_{\mathrm{dis}} \cdot \frac{\delta_2 - \delta_1}{D - 2d_{\mathrm{dis}}} - \delta_1\right)\cos\theta \tag{3}$$

$$x_{\mathrm{n}} = \frac{D - 2d_{\mathrm{dis}}}{\delta_2 - \delta_1} d_{\mathrm{m}} \tag{4}$$

$$j = (D + d_{\mathrm{c}})\cos\theta - \frac{x_n}{3} \tag{5}$$

where δ_1, δ_2 : displacements measured by the displacement sensors ($\delta_2 > \delta_1$), d_{dis}: distance from the wall edge to the displacement sensor axis, d_{c}: distance from the wall edge to the tensile force

In this study, following the CLT Manual [2], the center of compression force was assumed to be at $x_{\mathrm{n}}/3$. However, considering the embedment at the outer portion, the true center of compression is likely to be farther out than $x_{\mathrm{n}}/3$, which requires further investigation in future studies. Figure 5 compares the tensile force–uplift deformation relationships between the simple and rocking tensile tests with a wooden stopper. Here, the load-displacement relationship represents the average tensile force of each specimen at the same displacement. The angle bracket and HD hardware showed slightly higher values in the rocking tensile tests than in the simple tensile tests. The possible reasons for this include that the aforementioned assumption for the simplification of embedment behavior caused the actual moment arm length to be shorter than in reality, frictional force was generated at the contact surface between the hardware and wood due to the component of the tensile force acting on the bolt, and bending resistance occurred due to bolt bending. Subsequent discussions will focus on the rocking tensile tests, which more closely represent actual conditions.

Figure 6 shows the tensile force–uplift deformation relationships for specimens using the angle bracket and HD hardware. Comparing 910-HS-P and 1820-HS-P, which have different loading heights, reveals that the impact of loading height was minimal. Therefore, to examine the effect of the steel pipe on tensile

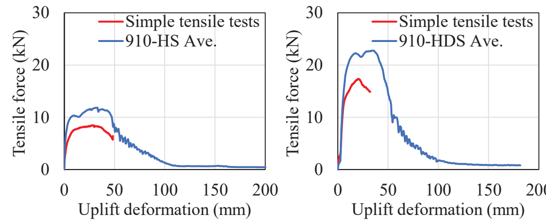

(a) Angle bracket (b) HD hardware

Figure 5. Load-displacement curves of simple and rocking tensile tests

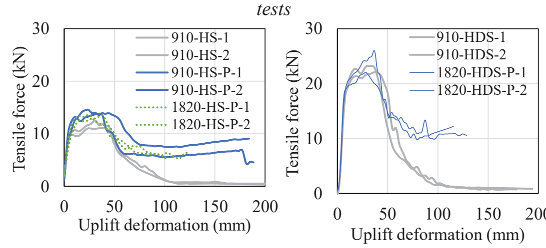

(a) Angle bracket (b) HD hardware

Figure 6. Load-displacement curves of rocking tensile tests

Table 2. Comparison of hardware properties between simple and rocking tensile tests (kN)

	T_{max}	T_{y}	T_{a}	Allowable capacity
910-HDS (Ave.)	22.8	13.3	13.3	20.4
Simple tensile (Ave.)	17.4	15.6	11.6	

performance, comparisons were made between 910-HS and 910-HS-P, 1820-HS-P, as well as between 910-HDS and 1820-HDS-P. Figure 6 indicates that tensile force remained even after the HD hardware detached in specimens with steel pipes. This residual resistance is attributed to frictional resistance generated in the localized embedment region between the steel pipe and CLT. At an uplift deformation of 100 mm, the residual tensile force was approximately 5–8 kN for 910-HS-P and 1820-HS-P with two steel pipes and 10–12 kN for 1820-HDS-P with four steel pipes, corresponding to 2.5–4.0 kN per steel pipe. Table 2 presents the maximum capacity T_{max}, yield capacity T_{y}, short-term standard capacity T_{a} in the simple and rocking tensile tests (910-HDS), and the short-term standard capacity from the manufacturer's joint performance test report [3] for the HD hardware. The value of T_{a} was defined as the smaller of $2/3T_{\mathrm{max}}$ and T_{y}. It should be noted that non-graded Japanese cedar lumber was used in the manufacturer's joint performance test. Due to installation on the cross-layer, a decrease in capacity was observed, and the short-term standard capacity of the HD hardware in the rocking tensile tests was 13.3 kN.

3 – FULL-SCALE STATIC LOADING TESTS

3.1 SPECIMEN

The four specimens were designated A1, A2, B1, and B2. As an example, Figure 7 illustrates the floor plan for each story and elevation for B1 and the shape of the column

https://doi.org/10.52202/080513-0010

head and orthogonal wall head hardware. The specimens have common dimensions: 6000 mm in the *X*-direction, 3000 mm in the *Y*-direction, and 2871 mm high from the top of the foundation to the top of the beam. In the Y2 plane, two types of CLT shear walls were used, with a height of 2481 mm and a width of 910 mm (1P) or 1820 mm (2P). The shear walls were 3 layer-105mm thick CLT panels of Japanese cedar (*Cryptomeria japonica*) with a strength grade of S60A according to Japan Agricultural Standard (JAS). The average Young's modulus of every lamina was equal to or more than 6.0 kN/mm^2. The orthogonal walls in the *Y*-direction were 90 mm thick, 1200 mm wide CLT panels with the same layer configuration, wood species, strength grade, and height as the CLT shear walls in the Y2 plane. The foundation was made of 105 mm square hinoki (*Chamaecyparis obtusa*) with no specific strength grading. The columns and beams were made of glued laminated timber of Scotch pine (*Pinus sylvestris*), according to JAS, with strength grades of E95-F315 for the columns and E105-F300 for the beams. The meaning of E95 is that the laminas in all layers have an average Young's modulus of 9.5 kN/mm^2 or greater, whereas F315 indicates that the bending strength of the glulam is 31.5 MPa. The second-floor diaphragm was covered with 24 mm thick structural plywood. The HS hardware (HDS) was installed at all four corners of the CLT shear walls. In the full-scale tests, the nuts of the HD were tightened with a wrench, ensuring an initial axial force. The shear joints of the CLT wall–foundation and the CLT wall–beam utilized steel pipes near the center of the walls, similar to the rocking tensile tests. The dowels were driven only into the foundation and beam and not fixed to the CLT shear walls.

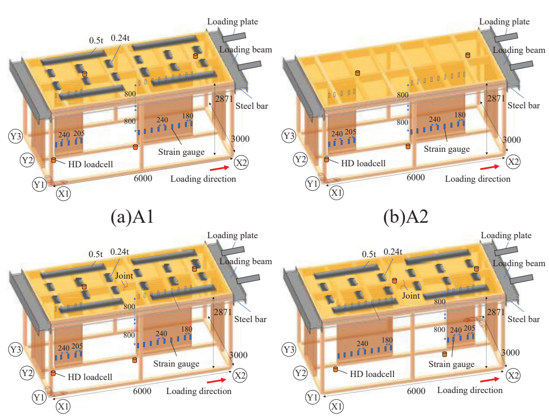

(a)A1 (b)A2

(c)B1 (d)B2

Figure 7. Diagram of the specimens

Table 3. Total specimen weight (kN)

	A1	A2	B1	B2
Wooden parts	16.6	16.2	16.8	16.3
Weights	47.9	0	47.9	47.9
Loading jig	17.74			
Total weight	82.1	33.8	82.3	81.8

The shear joints of the foundation–orthogonal wall and foundation–column were treated similarly, ensuring that they did not resist tensile forces. SPs were inserted at the beam–orthogonal wall shear joints, while other steel pipes (RP-10(+)) were inserted at the beam–column shear joints. The dowels were driven into both the walls (or columns) and beams, enabling resistance to tensile forces. Additionally, at the orthogonal wall heads, the hold-down hardware (HD-S14) with a two-pronged design was installed to securely fasten the orthogonal walls to beams, ensuring it was anchored to the parallel-layer lamina. The beam hangers were used at the beam-end joints, corresponding to a beam depth of 180 mm for the small beams and 390 mm for the large beams.

Specimen A series was designed to verify the difference in restoring force due to weight difference. For Specimen B series, a dovetail joint was introduced in the Y2 beam to examine the impact of joint presence on the vertical load distribution. The other specifications of B1 were the same as those of A1. For B2, the positions of the 1P and 2P walls were reversed compared to B1. Since loading was applied in a one-way direction, this configuration aimed to investigate differences in behavior due to loading direction. A hold-down hardware with a short-term capacity of 60kN (60kN HD) was installed at the beam center on both sides of the dovetail joints for B1 and B2 to prevent beam separation during loading. Table 3 presents the total weight of the specimens, including the wooden parts, loading jig, and weights. The weights were arranged as shown in the second-floor plan in Figure 7.

The design performance was based only on the allowable capacity of the HD hardware without considering the initial vertical load. The specimen's total weight was 82 kN, the wall width was 910 mm or 1820 mm, and the wall height was 2481 mm. When designing for an external force of 20% of the seismic weight using the allowable capacity of HD, the required capacity was calculated to be 10.4 kN. While further detailed discussion of the inflection height ratio is necessary, it was assumed to be 0.7 here. According to Table 2, the allowable capacity of the HD attached to the cross-layers of the CLT was approximately 13 kN, which is 1.25 times the required capacity. Although this hardware is somewhat overdesigned, the experiment was conducted under this specification. For A2, though there were no weights, the same HD hardware as the other three specimens was installed.

3.2 LOADING AND MEASURING METHOD

The loading was a one-way pull to the X2 side. However, in practice, as shown in Figure 7, the specimens were pushed using a loading girder on the X1 side, which was

https://doi.org/10.52202/080513-0010

linked with PC steel rods. While displacement transducers were also used for displacement measurement, this interstory drift includes vertical displacement components. Therefore, for experimental analysis, interstory lateral displacement was determined using image measurement with a high-resolution camera. To measure the tensile force of the HD hardware, load cells were installed at four locations: one at the top and one at the bottom of both the 1P and 2P walls. Additionally, strain gauges were attached to measure the axial force distribution of the 1P and 2P walls. Specifically, five strain gauges were attached to both the front and back of the upper and lower sections of the 1P wall, and nine were attached in the same manner to the 2P wall. The spacing of the strain gauges was primarily set at 240 mm to the left and right of the central gauge. However, the only outermost gauges were positioned at 10 mm from the edge of the wall.

3.3 LOAD-DISPLACEMENT CURVE AND SPECIMEN PERFORMANCE

The load-displacement curves of each specimen are shown in Figure 8. The overall behavior was that the load increased until the HD hardware was detached, followed by a gradual decrease in lateral force. The load reduction due to the bending failure of the beam, as shown in Figure 9(a), is more significant than that caused by the detachment of the HD hardware. As an example of the ultimate state, Figure 9(b) shows A1 pushing up the second-floor slab. It should be noted that while B1 collapsed, the loading on the other specimens was halted before collapsing for safety. B1 collapsed due to out-of-plane failure of the plywood in the lateral structure at an interstory drift of 1360 mm, which caused the CLT wall to overturn. The collapse limit was determined by assuming the intersection of the x-axis and the extension of the load-displacement curve. As a result, the collapse limits of A1, A2, and B2 were 1904 mm, 1844 mm, and 1872 mm, respectively, which were close to the wall width of 2P.

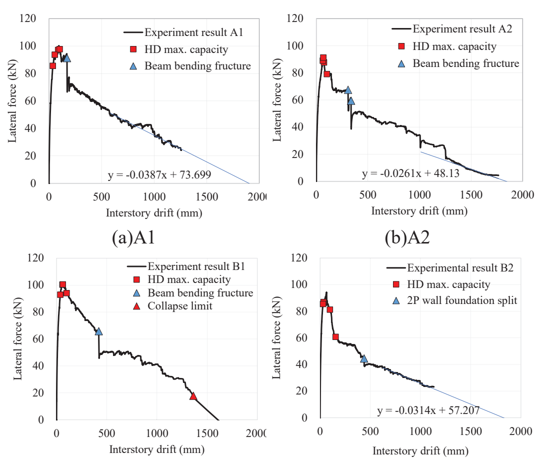

(a)A1 (b)A2

(c)B1 (d)B2

Figure 8. The load-displacement curve


(a) Interstory drift of 1262mm (b) Beam bending fracture

Figure 9. A1 at large deformation

Table 4 shows the maximum capacity $P_{\max}$, base shear capacity C_{B}, and the deformation at maximum capacity $D_{\max}$. Comparing A1 and A2, the vertical load difference was about 50 kN, but the maximum capacity was only about 8 kN different. The maximum capacity was almost the same for A1 and B1, where with or without the dovetail joint of the Y2 beam is the parameter. This is because the tensile force of the HD hardware installed at the dovetail joint provided bending resistance similar to that of a continuous beam. B1 and B2 differ in the loading direction, and B1 exhibited a higher maximum capacity of about 6 kN. Figure 10 shows the nearly collapsed state, where for B1, the 2P wall pushes up at the center, whereas for B2, it pushes up at the edge. Therefore, the lateral force also decreased since the axial force for the 2P wall was smaller for B2.According to the allowable stress design method [4], the short-term base shear capacity (allowable shear capacity) P_{a} for the shear wall is determined as the minimum value of the following indices: yield capacity P_{y}, $2/3\,P_{\max}$, the capacity at a deformation angle of 0.83% (P_{120}), 0.2 of the ultimate

Table 4. Maximum load P_{max}, Deformation at maximum load D_{max}

Specimen	A1	A2	B1	B2
$P_{\max}$ (kN)	100.3	91.9	100.8	94.3
$D_{\max}$ (mm)	94.1	71.0	62.6	63.4


(a)B1: At collapse (b) B2: Interstory drift 1131mm

Figure 10. B1 and B2 at large deformation

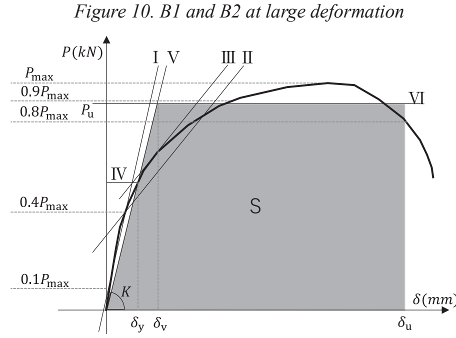

Figure 11. The calculation method of the structural indices

https://doi.org/10.52202/080513-0010

capacity P_u divided by the structural ductility factor (D_s). Figure 11 presents the calculation method of the structural indices. In addition, the allowable base shear capacity C_a was derived from the allowable capacity divided by the total weight of the specimens. These results are shown in Table 5. The allowable base shear capacity C_a exceeded 0.6 and was over 1.5 for A2 with no weights. The determining factor in all cases was P_y. The lateral resisting mechanism will be further analyzed in the next chapter based on the experimental results.

4 – DETAIL EXAMINATION OF THE EXPERIMENTAL RESULTS

4.1 LATERAL RESISTANCE BY HD HARDWARE

The load-displacement curves up to an interstory drift of 300 mm for each specimen are shown in Figure 12. The figure also includes the lateral resistance provided by the HD hardware. "-h" is added for the HD hardware at the wall head, and "-f" for that at the wall foot. The effective wall height during rocking h_e was determined using Equation (6), based on the wall width D, wall height $h(=2481mm)$, the distance from the wall edge to the displacement transducer $d_{dis}(=50mm)$, the deformation angle θ and the embedment depth d_m obtained from Equations (2) and (3). Additionally, the total lateral resistance provided by HD hardware was calculated from Equation (7) using the tensile force T for the four HD hardware and j derived from Equations (4) and (5). At the maximum load, the shear force provided by the HD hardware was approximately 40–50%, meaning that more than half of the resistance was provided by the restoring force. As previously mentioned, the base shear capacity C_B exceeded 0.6, which is a reasonable result, considering that HD hardware was somewhat overdesigned and that vertical load was not considered in the design process.

$$h_e = h\cos\theta + b\sin\theta - d_{m\,head} - d_{m\,foot} \tag{6}$$

$$Q = \sum Tj/h_e \tag{7}$$

Table 5. The properties and allowable capacity of each specimen

Specimen		A1	A2	B1	B2
P_y	(kN)	53.8	51.4	53.7	52.8
$2/3P_{max}$	(kN)	66.8	61.2	67.2	62.8
P_{120}	(kN)	72.5	64.3	79.9	81.4
$0.2P_u\sqrt{2\mu-1}$	(kN)	71.8	55.0	97.2	68.4
Allowable capacity P_a	(kN)	53.8	51.4	53.7	52.8
C_a (P_a / total weight)		0.66	1.52	0.65	0.65

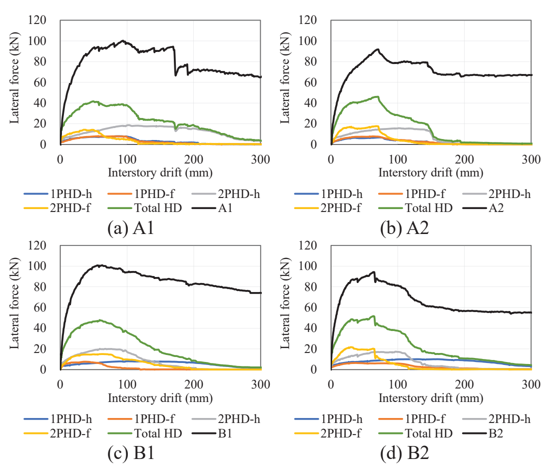

Figure 12. The load-displacement curves and lateral resistance of HD hardware – interstory drift relationship

4.2 THE VERTICAL LOAD DISTRIBUTION

Figure 13 provides the strain distribution of the CLT shear wall for A1 at 0.83% (1/120 rad), P_{max}, 10% (1/10 rad), and 33.3% (1/3 rad). At 0.83%, tensile strain due to the HD hardware was recorded, and at P_{max}, the maximum tensile strain was observed at locations other than the 2P wall foot. No tensile strain was observed at 10% as the HD hardware had already detached. The compressive strain was observed at the corners in contact with the foundation and beam, confirming the formation of a compression strut. The axial force for each wall was then calculated. As shown in Figure 14, the strain value ε_i measured by each strain gauge, the representative width b_i corresponding to each gauge, the CLT thickness t(105 mm), and the deformation angle θ were defined. The Young's modulus E (between 5.31 and 5.82 kN/mm²) was determined from full-surface compression tests conducted on specimens cut from the CLT shear

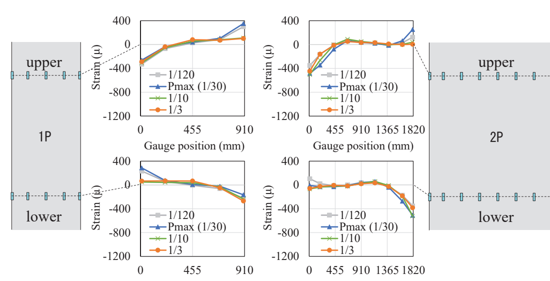

Figure 13. The strain distribution of each wall for A1

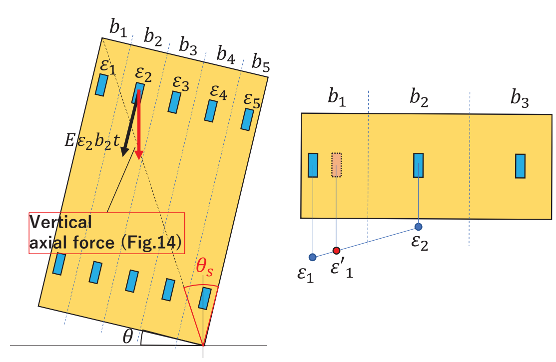

Figure 14. The way of calculating the axial force

walls used in the full-scale static loading tests. The diagonal angle θ_s was used for calculating the axial force of the strut in Section 5.2. Since the outermost strain gauge was not positioned at the center of the cooperative width, its strain value ε'_i was obtained via linear interpolation using the adjacent gauge values. In the full-scale tests, the zero of the strain gauges was taken immediately before loading commenced, meaning the gauges measured fluctuating axial forces. Therefore, defining the number of gauges per row as $n(=5, 9)$, the vertical force N at both the upper and lower sections of the walls was calculated using Equation (8), and the average of these values was taken as the fluctuating axial force for the walls. The total vertical axial force of the CLT shear walls was determined by adding the long-term axial force, calculated while considering the load-bearing area, as shown in Figure 15. The weight of the loading jig was primarily borne by the vertical members in the X1 and X2 planes, so its weight was excluded from the long-term axial force calculations.

$$N = \left(\sum_{2}^{n-1} E\varepsilon_i b_i t + E\varepsilon'_1 b_1 t + E\varepsilon'_n b_n t \right) / \cos\theta \qquad (8)$$

Figure 16 illustrates the transition of vertical axial force for each wall. Additionally, the total weight of each specimen is indicated in the figure. The vertical axial force for the walls initially increased in a nonlinear manner. Subsequently, the axial force surpasses the total weight of the specimens, which was 34 kN for A2 and 82 kN for the other specimens, by approximately 35 kN.

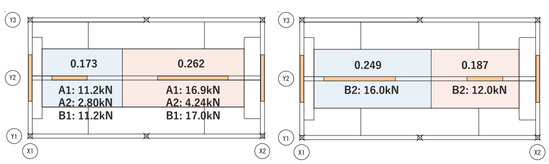

(a) A1, A2, B1 (b) B2

Figure 15. The load-bearing area for the CLT walls

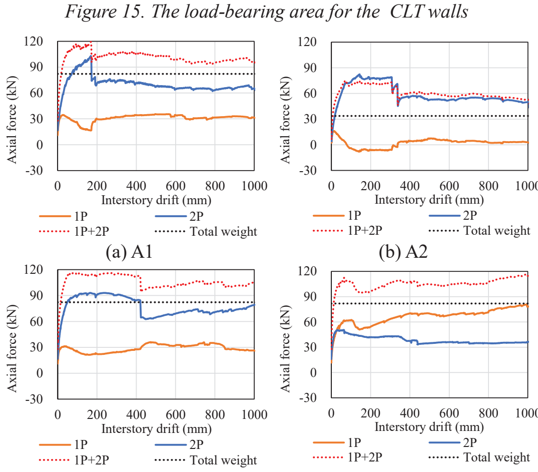

(a) A1 (b) A2

(c) B1 (d) B2

Figure 16. The transition of axial force

This increase is attributed to the presence of steel pipes installed in both the 1P and 2P walls, which were previously noted to provide a tensile resistance of 2.5–4.0 kN per pipe. For all specimens, beyond a deformation of approximately 300 mm, the axial force remains relatively stable with minor fluctuations. Except for B2, the initial axial force for the 2P wall exceeds the 2:1 ratio of its length proportion relative to the 1P wall. However, the axial force distribution tends to align more closely with this length ratio at larger deformation. Nevertheless, each specimen exhibits distinct tendencies. For A2, which was not subjected to weights, the 2P wall is dominant, while the 1P wall bearing no vertical load contributes minimally to lateral force resistance. For B2, as mentioned earlier, the influence of wall arrangement and loading direction resulted in the 1P and 2P walls carrying nearly equal loads up to a deformation of approximately 200 mm.

5 – ANALYSIS METHOD

The analysis was conducted using the extended distinct element method (EDEM)-based analysis software "wallstat". As an example of the analysis model, Figure 17 illustrates the analysis model of B1 and the modeling of the CLT shear walls in the Y2 plane. Figure 18 presents the modeling method for joints, while Figure 19 shows the arrangement of springs in the Y2 plane. The CLT shear wall was modeled using compression springs (C8) to represent the compression struts formed during rocking, along with rigid truss elements of the same length as the wall height and rigid beams of the same length as the wall width. Since compression struts are not formed in orthogonal walls, these walls were modeled using beam elements of the same length as the wall height with rigid beams of the same length as the wall width attached to both ends. Columns and beams were modeled as beam elements. At the four corners of the CLT shear wall, tensile springs (T1) were installed to simulate HD hardware, and additional tensile springs (T2) were used to represent the tensile resistance of the steel pipe. Though this will be discussed later, it should be noted that the installation positions of the hardware in the experiment and the positions of the springs in the analysis differed; therefore, the parameters in the analysis were determined considering this difference. The tensile joints at the beam–orthogonal wall and the beam–column using HD-S14 were modeled with rigid tensile springs (T3). Since the steel pipes at the foundation–orthogonal wall and foundation–column were designed not to resist tension, no tensile springs were assigned. For the shear joints at the shear wall–beam and the shear wall–foundation, rigid shear springs (S1) were placed at two points at the corners of the CLT shear wall where it was

https://doi.org/10.52202/080513-0010

in contact with either the foundation or the beam to express friction. Furthermore, the nodes at the four corners of the wall were fixed in the Y direction to prevent out-of-plane rotation of the shear wall. Rotational springs (R) were placed at the beam-end joints, and sensitivity analysis was performed by considering two stiffness conditions: pinned (hereafter, p-end) and rigid (hereafter, r-end). Similarly, for the dovetail joint of the specimen B series, sensitivity analysis was performed by considering two stiffness conditions: pinned dovetail joints (hereafter, p-joint) and rigid dovetail joints (hereafter, r-joint). In the r-joint model, compression springs (C7) were placed 195 mm above and below the beam center to represent the compression between beams, while a rigid tensile spring (T3) was placed at the beam center to simulate 60kN HD. Additionally, rigid shear springs (S2) were used to model friction and the shear resistance of the dovetail joint, and these elements were connected with rigid beams. In the p-joint model, the stiffness of the compression springs at the top and bottom of the beam was set to 1N/mm, and a new rigid compression spring was introduced at the beam center for axial force transmission.

The definitions of each parameter are summarized in Table 6. The backbone curve of the tensile spring (T1), which corresponds to the HD hardware at the CLT shear wall–beam and CLT shear wall–foundation, is shown in Figure 20(a). The tensile force measured in the full-scale tests for each HD hardware was corrected to the tensile force at the wall edge by multiplying it by the ratio of the

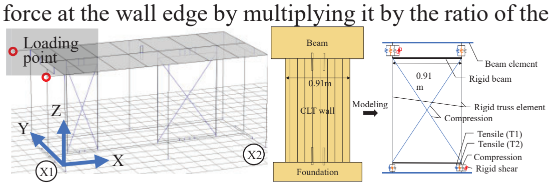

Figure 17. analysis model(B1), modeling of CLT wall

Table 6. The list of parameters

Symbol	Parameter name	Linear or not	Species	Definition
T1	HD hardware at CLT joint	Non-linear	Tensile	From Chapter 3
T2	Tension of steel pipe at CLT joint	Non-linear	Tensile	From Chapter 2
T3	Tension of dovetail joint and orthogonal wall head and column head	Linear	Tensile	Rigid
S1	The friction of CLT－beam and CLT－foundation	Linear	Shear	Rigid
S2	Shear of head and foot of orthogonal wall and column	Linear	Shear	Rigid
C1–C6	Embedment of CLT	Non-linear	Compression	[13]
C7	Stiffness between beams at the dovetail joint	Linear	Compression	Rigid or 1N/mm
C8	Compression strut stiffness	Linear	Compression	[16]
	Column and beam	Non-linear	Beam element	[17-19]
S1, T3, C7	Rotation stiffness of the dovetail joint	Linear	Combination	Rigid or Pin
R	Rotation stiffness of the beam end joints	Linear	Rotation	Rigid or Pin

stress center distance to the orthogonal projection of the wall width ($j/D\cos\theta$). The uplift deformation was also corrected to the deformation at the wall edge by dividing it by ($j/D\cos\theta$). The backbone curve was defined as a tetralinear model, also considering the HD hardware's initial axial force. The backbone curve of the tensile spring (T2), which represents the tensile resistance of the steel pipe, is shown in Figure 20(b). The load-displacement curve for two steel pipes was obtained by subtracting the load-displacement curve without the steel pipe from that with the steel pipes in the rocking tensile tests, with corrections because of the spring arrangement at the wall edge similar to the HD hardware. The initial and secondary stiffness was adjusted according to the number of steel pipes used in the 1P wall and 2P wall. Since the steel pipes were averagely positioned at the center of the wall in the full-scale tests, the ultimate displacement was determined so that the tensile spring at the wall edge would fail at the same deformation angle as the case at the center of the wall. The tensile resistance at the ultimate displacement was set to zero. The shear stiffness of the steel pipes (S2) at the head and foot of columns and orthogonal walls was considered rigid. The performance of the embedment (C1–C6) of the CLT shear wall and orthogonal wall into the beam and foundation was determined to assume that one-quarter of the wall width contributes to the embedment. The stiffness of the compression spring (C8), which represents the compression strut in the CLT shear wall, was determined by calculating the compression strut width and Young's modulus of CLT in the strut direction [5]. The Young's modulus in the major axis of each CLT shear wall was the same as in Section 4.2. The Young's modulus of the beam elements for the orthogonal walls was set to the standard value of 4.0kN/mm^2. Young's modulus of the columns and beams was set to 9.5

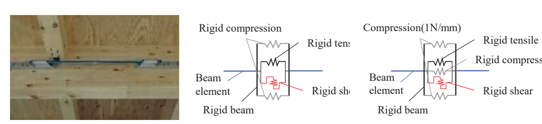

(a) Dovetail joint (b) Case of rigid (c) Case of pin

Figure 18. Modeling of the dovetail joints

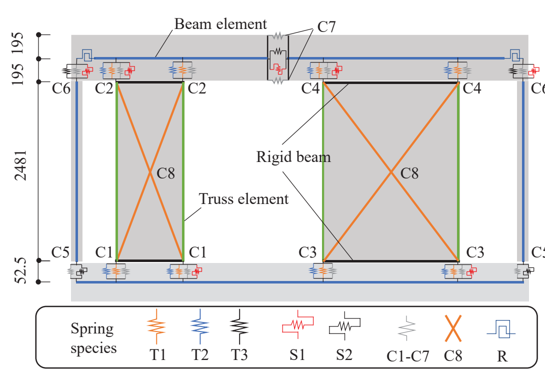

Figure 19. Spring arrangements in the Y2 plane for B1

kN/mm² and 10.5 kN/mm², respectively [6]. The bending strength was determined by multiplying the standard strength values of 31.5 N/mm² and 30.0 N/mm² by a safety factor of 1.3 [7].

The weight distribution is summarized in Table 7. The weight of the wooden parts shown in Table 3 was distributed to each Y plane (Y1, Y2, Y3) according to the density and volume of the structural members within the cooperative width. The weight of the weights was also distributed according to the cooperative width of each Y plane. Additionally, the total weight of the loading girder and steel rods (16.52 kN) was evenly distributed to the beams in the X1 and X2 planes. The weight of the loading plate (1.12 kN) was assigned to the beam in the X2 plane. The loading was modeled as push loading from the X1 side in this analysis because the specimens were pushed using a loading girder on the X1 side in the experiments. The displacement increment was applied to the endpoints (loading points in Figure 17) of the two rigid beams extending in the X direction from the beam in X1.

6 – ANALYSIS RESULTS

The load-displacement curves from the full-scale tests and the analysis are shown in Figure 21. Except for the sudden load drop in A2, the results assuming r-end generally captured the overall behavior. Regarding P_{max}, the experimental results were generally between the analytical results of the p-end and r-end models. At an interstory drift of approximately 1000 mm, the analysis exhibited lower capacity than the experiment. Due to embedment effects and other factors, the effective wall width was reduced, decreasing the collapse limit in the experiment. However, the specimens maintained structural integrity, possibly due to steel pipes in orthogonal walls and columns that were not considered in the analysis.

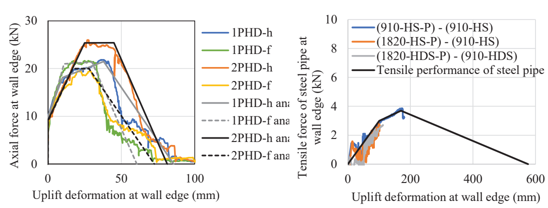

(a) HD hardware for A1 (b) Steel pipe

Figure 20. The backbone curve of HD hardware and steel pipe on tensile performance

Table 7. The weight for each plane (unit:kN)

	A1	A2	B1	B2
Y2 (weights)	28.2	0	28.2	28.2
Y1, Y3 (weights)	9.81	0	9.81	9.81
Y2 (wooden parts)	10.62	10.37	10.75	10.43
Y1, Y3 (wooden parts)	2.99	2.92	3.02	2.93
X1	8.26			
X2	9.38			
Total weight	82.1	33.8	82.3	81.8

For B1 and B2 with either r-jont or p-joint, Figure 22 shows the moment diagram when the 2P wall carries maximum axial force and the arrows expressing the weight transmission presumed from the moment diagram. It was confirmed that significant weight was supported at the uplift position of the rocking wall. It was also confirmed analytically that more weight was transferred to the uplift position, which was the 2P wall, in r-end compared with p-end. For B2, the difference in lateral resistance between the p-joint and r-joint cases was small. As shown in Figure 10, the uplift position of the 2P wall in B2 was located at the perimeter, and the centrally located 1P wall exhibited less uplift than the 2P wall.

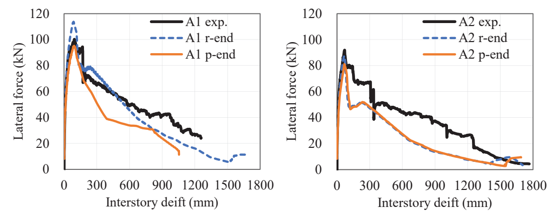

(a)A1 (b)A2

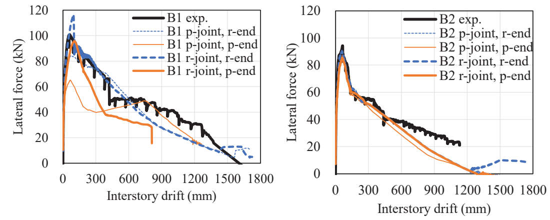

(c)B1 (d)B2

Figure 21. Comparison of load-displacement curves between the experiment and analysis

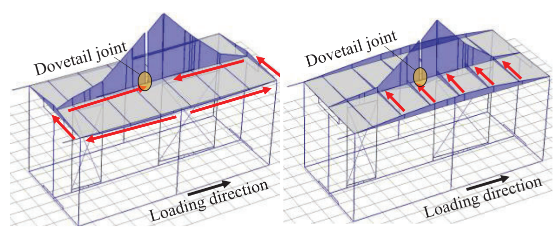

(a)B1 with r-joint and p-end (b)B1 with r-joint and r-end

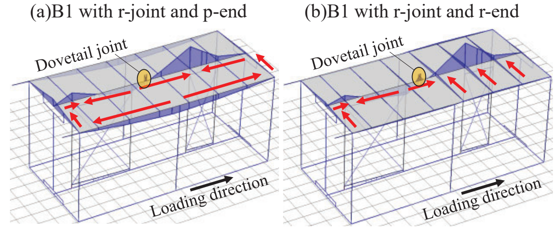

(c)B2 with r-joint and p-end (d)B2 with r-joint and r-end

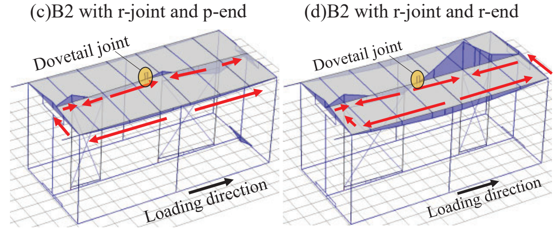

(e)B1 with p-joint and p-end (f)B2 with p-joint and p-end

Figure 22. Moment diagram at maximum axial force of 2P wall and transmission path of weight

https://doi.org/10.52202/080513-0010

Consequently, the influence of beam-end rotational stiffness on lateral resistance was smaller in B2 than in B1. Furthermore, moments were observed at the dovetail joint in B1 with the r-joint, on the other hand, they were nearly zero in B2 with r-joint. Therefore, significant differences in the moment diagram and load-deformation behavior were observed between the r-joint and p-joint in B1, whereas such differences were not observed in B2.

7 – CONCLUSION

To obtain fundamental insights into the lateral resisting mechanism and collapse limit of single-story CLT shear wall structures using hardware for conventional wooden houses, loading was applied until the inter-story drift angle exceeded 33%. As a result:

- The collapse limit of the specimens was exceeded by approximately 1000 mm (about 33%).
- The allowable base shear capacity exceeded 0.6.
- As deformation progressed, the axial force for the CLT shear walls was different from the long-term axial force state. The axial force stabilized as the weight transferred to the CLT shear wall after an interstory drift of 300 mm when the CLT shear wall exhibited rocking behavior and stood on one side.

To clarify the vertical load transmission mechanism to CLT rocking shear walls, which is crucial for restoring force, an analysis was performed by assuming the rotational stiffness of the beam-end joints and dovetail joints on the Y2 beam as either pinned or rigid, and the results were compared with experimental results.

- Except for the p-joint B1, the analysis assuming r-end generally agreed with the overall load-deformation behavior, and the experimental results fell between the p-end and r-end analyses in terms of initial stiffness and $P_{\max}$.
- As deformation progressed and the CLT shear wall uplifted, the axial force carried by the more centrally positioned CLT shear wall increased and deviated from the long-term axial force state.
- The sensitivity of the load-displacement curve to the rotational stiffness of beam-end joints and dovetail joints varied depending on the arrangement of the CLT rocking shear walls.

Future works will include shake table tests to further investigate the seismic resisting mechanism and collapse limit of this structural system.

8 – ACKNOWLEDGEMENT

This research was subsidized by the "FY2022 project to improve the environment for the use of CLT, LVL, etc. in buildings, and to reduce costs and verify the use of CLT, LVL, etc. in Buildings" as part of the measures to strengthen the supply and use of lumber for construction purposes. We would like to express our gratitude to all parties involved.

9 – REFERENCES

[1] S. Momose, T. Nakagawa, T, Namba, H. Isoda, T. Miyake. “An Analytical Method to Reproduce Seismic Behavior of a Two-Story Cross-Laminated Timber Building at Large Deformation.” In: J. of Struct. Eng. 149(6), 2023. DOI: https://doi.org/10.1061/JSENDH.STENG-11711.

[2] Japan Housing and Wood Technology Center. 2016. Design and construction manual for CLT buildings. Koutou ward, Tokyo: Japan Housing and Wood Technology Center.

[3] BX Kaneshin. Co., Ltd., “BX Kaneshin. Co., Ltd. -Building hardware-”, https://www.kaneshin.co.jp/, (17/02/2025)

[4] MLITT (Ministry of Land, Infrastructure, Transport and Tourism). 2008. Allowable stress design method of conventional buildings. [In Japanese.] Tokyo: Japan Housing and Wood Technology Center.

[5] K. Fukumoto, H. Isoda. “Study on The Quantification of Horizontal Stiffness and Compression Strut of CLT Seismic Panels Infilled Within A Steel Frame”, Vol. 89 (818), pp. 451-461, 2024. [In Japanese] DOI: https://doi.org/10.3130/aijs.89.451.

[6] Architectural Institute of Japan. “Standard for Structural Design of Timber Structures -Allowable Stress, Allowable Capacity Design-”, 2013.

[7] T. Kikuchi, N. Yotsumoto, F. Kawarabayashi, Y. Nakayama, M. Totsuka, T. Hirashima. “Experimental Study on Fire Performance of Glulam Timber Frames (Part 2): Bending Resistance and Deflection Behavior of The Cedar Beams with Dowel-Type Connections in Fire”, J. Struct. Constr. Eng., AIJ, 88(810), pp.1306-1317, Aug., 2023. [In Japanese] DOI: https://doi.org/10.3130/aijs.88.1306.